

# Solid-state Thermoelectric Characteristics of NiII, FeII, CoII, and CuII Borohydrides

Isam M. Arafa (✉ [isamaraf@just.edu.jo](mailto:isamaraf@just.edu.jo))

Jordan University of Science and Technology <https://orcid.org/0000-0001-9231-4098>

Mazin Y. Shatnawi

Department of Applied Chemistry, Faculty of Science and Arts, Jordan University of Science and Technology, P.O. Box 3030, Irbid 22110, Jordan

Yousef N. Obeidallah

Department of Applied Chemistry, Faculty of Science and Arts, Jordan University of Science and Technology, P.O. Box 3030, Irbid 22110, Jordan

Ahmed K. Hijazi

Department of Applied Chemistry, Faculty of Science and Arts, Jordan University of Science and Technology, P.O. Box 3030, Irbid 22110, Jordan

Yaser A. Yousef

Department of Chemistry, Yarmouk University, Irbid, Jordan

---

## Research Article

**Keywords:** metal borohydrides, thermoelectricity, energy harvesting, waste heat, Seebeck, figure of merit, power factor

**Posted Date:** May 17th, 2021

**DOI:** <https://doi.org/10.21203/rs.3.rs-521859/v1>

**License:**  This work is licensed under a Creative Commons Attribution 4.0 International License.

[Read Full License](#)

---

# Solid-State Thermoelectric Characteristics of Ni<sup>II</sup>, Fe<sup>II</sup>, Co<sup>II</sup>, and Cu<sup>II</sup> Borohydrides

Isam M. Arafa<sup>a\*</sup>, Mazin Y. Shatnawi<sup>a</sup>, Yousef N. Obeidallah<sup>a</sup>,  
Ahmed K. Hijazi<sup>a</sup>, Yaser A. Yousef<sup>b</sup>

<sup>a</sup> Department of Applied Chemistry, Faculty of Science and Arts, Jordan University of Science and Technology, P.O. Box 3030, Irbid 22110, Jordan.

<sup>b</sup> Department of Chemistry, Yarmouk University, Irbid, Jordan

\* Corresponding Author, Fax: 962-2-7201071, E-mail: [isamaraf@just.edu.jo](mailto:isamaraf@just.edu.jo)

---

## ABSTRACT

Four transition metal borohydrides (M<sub>T</sub>BH<sub>4</sub>, M<sub>T</sub> = Ni, Fe, Co, and Cu) were prepared by sonicating a mixture of the desired M<sub>T</sub> salt with excess NaBH<sub>4</sub> in a nonaqueous DMF/CH<sub>3</sub>OH media. The process afforded bimetallic (Ni-BH<sub>4</sub>), trimetallic (Fe-BH<sub>4</sub>, Co-BH<sub>4</sub>), and mixed-valence (Cu-H, Cu-BH<sub>4</sub>) amorphous, ferromagnetic nanoparticles as identified by thermal, ATR-IR, X-Ray diffraction, and magnetic susceptibility techniques. The electrical conductivity ( $\sigma$ ) of cold-pressed discs of these M<sub>T</sub>BH<sub>4</sub>s shows a nonlinear increase while their thermal conductivity ( $\kappa$ ) decreases in the temperature range of  $303 \leq T \leq 373$  K. The thermal energy transport occurs through phonon lattice dynamics rather than electronic. The  $\sigma/\kappa$  ratio shows a nonlinear steep increase from 9.4 to 270 KV<sup>-2</sup> in Ni-BH<sub>4</sub>, while a moderate-weak increase is observed for Fe-BH<sub>4</sub>, Co-BH<sub>4</sub>, and Cu-BH<sub>4</sub>. Accordingly, the corresponding thermoelectric (TE) parameters S, PF, ZT, and  $\eta$  were evaluated. All TE data shows that the bimetallic Ni-BH<sub>4</sub> (S, 80  $\mu$ VK<sup>-1</sup>; PF, 259  $\mu$ Wm<sup>-1</sup>K<sup>-2</sup>; ZT 0.64;  $\eta$ , 2.56%) is a better TE semiconductor than the other three M<sub>T</sub>-BH<sub>4</sub>s investigated in this study. Our findings show that Ni-BH<sub>4</sub> is a promising candidate to exploit low-temperature waste heat from body heat, sunshine, and small domestic devices for small-scale TE applications.

---

**Keywords:** metal borohydrides, thermoelectricity, energy harvesting, waste heat, Seebeck, figure of merit, power factor.

## 1.0 Introduction

Current research and commercialization on renewable energy focus mainly on solar photovoltaic (**PV**), geothermal, and wind sources as viable energy sources for large-scale electricity production [1-2]. However, to a much lesser extent was the interest in utilizing waste heat through thermoelectric (**TE**) techniques [3-27]. In this straight-forward technology, the temperature gradient ( $\Delta T$ ) is directly related to the induced DC thermal voltage ( $\Delta V$ ) and *vice-versa* as described by Seebeck power function (1) and Peltier refrigeration functions (2),

$$\Delta V = - S (\Delta T) \quad (1)$$

$$Q = \Delta\pi (I) \quad (2)$$

where  $S$ ,  $\Delta\pi$ ,  $Q$ , and  $I$  are the Seebeck coefficient, difference in Peltier factors, heat, and electric current, respectively [3,11-13]. However, the ability of a material to produce TE power is determined by its power factor (**PF**), and the dimensionless figure of merit (**ZT**), **Equations 3** and **4**.

$$PF = (\sigma) S^2 \quad (3)$$

$$ZT = (\sigma/\kappa) S^2 T \quad (4)$$

Although TE technology is direct, simple, and environmentally friendly, its sluggish progress over the past few decades is partly due to the lack of efficient TE semiconducting materials and the low conversion efficiencies ( $\eta < 5\%$ ) [4-7,11-15,20-23]. Nevertheless, for TE technology to be practically viable and competitive with PV technology for harvesting solar energy, the TE semiconductors should exhibit ZT values  $\geq 1$  or PF  $\geq 4$  mW/m.K<sup>2</sup> [3,4,7,11-15]. Today, TE technology development becomes a top priority to harvest waste heat associated with fuel engines, small domestic devices, solar thermal radiation, and other heat sources. Current research in this field is unfolding on utilizing solar thermal energy to build solar-based TE systems [24,25]. However, the success of this technology relies on obtaining

p-type and n-type TE semiconductors that are characterized by narrow bandgap exhibiting sufficiently high  $\sigma$  and  $S$  values while displaying low  $\kappa$  [3-7,11-19,20-23]. Recent reports showed that the microstructure of TE materials as displayed by the grain size and morphology (texture, crystallinity, dimensionality) significantly affect the transport of charge carriers and phonons scattering. Different authors showed that the  $\kappa$  could be reduced through grain boundary scattering, phonon-glass electron crystals, formation of nanocomposites, and introduction of sublattice crystalline defects. At the same time,  $\sigma$  can be enhanced through low dimensional structure, structural modification, and increase charge carrier concentration [4,6,7,20-23]. In this respect, polycrystalline materials with a large-sized grain ( $> 2 \text{ mm}$ ) offer transport pathways for electrons but cannot scatter phonons efficiently at the interfaces, resulting in increasing  $\sigma$  and  $\kappa_{\text{lattice}}$  as well. On the contrary, nanoscale grains particles ( $>500 \text{ nm}$ ) scatter phonons to maintain a low  $\kappa_{\text{lattice}}$  while the  $\sigma$  increases, thus enhancing ZT values. These findings also showed that the carrier mobility can be enhanced through microstructure where 1-D linear and 2-D layer structural arrays are preferred to 3-D bulk materials.

To date, the quest for new n-type and p-type semiconductors, composites, and C-based materials for TE applications continue [8-19,22,27]. However, inorganic TE semiconductors are generally classified as metal chalcogenides ( $\text{Bi}_2\text{Te}_3$ ,  $\text{Bi}_2\text{Se}_3$ ,  $\text{PbTe}$ ,  $\text{SnSe}$ ,  $\text{MoSe}_2/\text{MoS}_2\dots$ ), metal oxides ( $\text{LaMo}_8\text{O}_{14}$ ,  $\text{ZnO}$ ,  $\text{Na}_x\text{Co}_2\text{O}_4$ ,  $\text{Ca}_3\text{Co}_4\text{O}_9$ ,  $\text{CaMnO}_3$ ,  $\text{SrTiO}_3$ ,  $\text{In}_2\text{O}_3$ ), borides ( $\text{ZrB}_2$ ,  $\text{HfB}_2$ ), lead-based perovskites ( $\text{CH}_3\text{NH}_3\text{PbI}_3$ ), and others ( $\text{Si}_{1-x}\text{Ge}_x$ ) [3,8-10,26,27]. The highest PF value of  $2.8 \text{ mW/m.K}^2$  at  $773 \text{ K}$  was reported for n-type  $\text{SnSe}$  semiconductor. On the other hand, interest in C-based materials, including  $\text{C}_{\text{graphite}}$ ,  $\text{C}_{\text{nanotube}}$ ,  $\text{C}_{\text{graphene}}$  nanoparticles, and thin films, is constantly rising [12-19]. The highest reported PFs for such nanoparticles are within  $2.71$  and  $2.46 \text{ mW/mK}$  for p-type and n-type, respectively. Recently, Kanahashi *et al.* reported still higher PF values for p-doped ( $6.93 \text{ mW/mK}$ ) and n-doped ( $3.29 \text{ mW/mK}$ )

graphene films [19]. This class is extended to their composites with conducting polymers (PEDOT, PANI,...) [12-15].

On the other hand, metal borides (**M-Bs**) [26-34] and metal borohydrides (**M-BHs**) [35-45] of p-, d-, and f-block elements have become in the spotlight as solid-state materials. Nevertheless, these two classes of materials are closely related where M-BHs undergo dehydrogenation to yield M-Bs when subjected to heat (300-400 °C) under an inert atmosphere [35-38,40]. These M-Bs are generally classified as boron-rich ( $MB_{12}$  -  $MB_{70}$ ) and metal-rich ( $M_2B$ -to-  $M_5B$ ), exhibiting a variety of structures, including isolated B atoms, chains, layer, and clusters [26-34]. Currently, the exceptional structural, hardness and thermal properties of M-Bs receive increasing attention as hard refractory ( $TiB_6$ ), hard magnets ( $Nd_2Fe_{14}B$ ), battery electrodes, conducting ceramics ( $ZrB_2$ ,  $HfB_2$ ), electro-catalysis, and superconducting ( $MgB_2$ ) materials [26-34]. Meanwhile, solid-state M-BHs continue to attract attention as H-storage materials in solid fuels, electrolytes in batteries, and luminescence and magnetic applications [35-42]. Given these characteristics, both M-BHs and M-Bs are anticipated to play a key role in the future's sustainable energy. Although  $M_T$ -Bs and M-BHs tend to form thermally stable materials, their utilization in TE applications is limited [26,27]. Our current research is directed towards the synthesis and applications of materials that possess the potential to convert low-temperature heat ( $303 \leq T \leq 373$  K) resulting from body heat, sunshine, and domestic devices for small-scale TE applications. This work reports the synthesis, characterization, and utilization of four transition metal borohydrides ( **$M_T$ -BH<sub>4</sub> = Ni-BH<sub>4</sub>, Fe-BH<sub>4</sub>, Co-BH<sub>4</sub>, Cu-BH<sub>4</sub>**) semiconductors for TE applications. The  $M_T$ -BHs were prepared by mixing and sonicating the transition metal salts with NaBH<sub>4</sub> in the DMF/MeOH mixed solvent system. The individual products were characterized by thermo-oxidative, vibrational spectroscopy (**ATR-IR**), X-Ray diffraction (**P-XRD**), and magnetic ( $\mu_{eff}$ ) techniques. The thermal ( $\kappa$ ), electrical

( $\sigma$ ) conductivities and the corresponding TE parameters (**S**, **PF**, **ZT**) were evaluated at ambient conditions.

## 2.0 Materials and Methods:

All chemicals and solvents were reagent grade and used as received unless otherwise stated ( $\text{NiCl}_2 \cdot 6\text{H}_2\text{O}$ , Aldrich;  $\text{CoCl}_2 \cdot 6\text{H}_2\text{O}$ , Janssen Chimica;  $\text{CuCl}_2 \cdot 2\text{H}_2\text{O}$ , Scharlau;  $\text{FeSO}_4 \cdot 7\text{H}_2\text{O}$ , Codex;  $\text{NaBH}_4$ , Aldrich). Prior to each preparation, the transition metal salts were soaked in absolute alcohol for ~10 min., decanted, and dried. This step helps to minimize the presence of water in the reaction system. Thermo-oxidation was performed in a muffle furnace (open-air, steps of 100 °C,  $25 < T < 1100$  °C). The magnetic susceptibility measurements were carried out using a Sherwood Static magnetic susceptibility balance. The P-XRD was performed on a RIGAKU ( $\text{Cu}_\alpha \lambda = 1.5408$  Å, 40 kV, 40 mA, K- $\beta$  filter, scintillation counter, scan speed = 3.00 deg./min. sampling width: 0.0200 deg, Scan range  $2\theta = 5.00 - 90.00$  deg.). The positions of the diffraction peaks were determined by RIGAKU curve-fitting software. The ATR-IR spectra were recorded using a Bruker ATR-IR (Alpha, OPUS-7.5.1.8) spectrometer (Range: 4000-400  $\text{cm}^{-1}$ , Scans: 24, Resolution: 4  $\text{cm}^{-1}$ ). The TE characteristics of the products were performed on cold-pressed circular discs (10 ton/ $\text{cm}^2$ , 2 minutes, radius = 6.51 mm, area,  $\pi r^2 = 1.33 \times 10^{-4}$   $\text{m}^2$ , thickness 1-1.1 mm) of 0.500 g of dry fine samples, sandwiched between two polished brass electrodes, **Figure 1**. The lower brass disc was gradually heated, and the  $\Delta T$  between the two brass discs was monitored using a digital K-type thermocouple. The developed voltage ( $\Delta V$ ) was monitored as a function of ( $\Delta T$ ) in the range of 300-373 K using a digital K-type multimeter and thermocouple. Thermal conductivity ( $[\kappa = Q/((\Delta T/L) * A)]$ ,  $\text{WK}^{-1}\text{m}^{-1}$ ) was evaluated from the heat flux ( $Q$ , W) passing from the hot disc to the cold disc through  $M_T$ -BHs discs. Electrical conductivity ( $\sigma$ ,  $\text{Siemen m}^{-1}$ ) was determined

for nonohmic behavior from  $\ln I$  vs.  $\ln V$  plot where the intercept gives  $\ln G$  (conductance,  $[G = A * \sigma / L]$ ).

### **Figure 1: Device for thermoelectric properties.**

## **2.1 Synthesis of Transition Metal *Borohydride* ( $M_T$ -BHs):**

### **2.1.1 Nickel *Borohydride* (Ni-BH<sub>4</sub>)**

A freshly prepared solution of NaBH<sub>4</sub> (1.513 g, 40 mmol) in 50 mL of methanol was dropwise added within 15 min. to a solution of NiCl<sub>2</sub>·6H<sub>2</sub>O (2.377 g, 10 mmol) dissolved in 50 mL of DMF. The reaction mixture was sonicated for 90 min. at about 70 °C. The obtained Ni-BH<sub>4</sub> precipitate was filtered off, washed with distilled water and acetone, dried in an oven (80 °C, 12 hrs.), and stored under vacuum for further analysis. Yield = 56%; Color/State: lustrous black solid. Density cold-pressed disc: 2.72 g/cm<sup>3</sup>. **ATR-IR:** 3350 (br,  $\nu_{O-H}$ ); 2073 (m,  $\nu_{B-Ht}$ ); 2002 (m,  $\nu_{B-Hb}$ ); 1149 (w,  $\delta_{BH2}$ ); 470 (w,  $\nu_{\text{asym Ni-HBH}}$ ) cm<sup>-1</sup>.

### **2.1.2 Copper *Borohydride* (Cu-BH<sub>4</sub>):**

The **Cu-BH<sub>4</sub>** was prepared and isolated as described above employing CuCl<sub>2</sub>·2H<sub>2</sub>O (1.34 g, 10 mmol) and NaBH<sub>4</sub> (1.513 g, 40 mmol). Yield = 55%; Color / State: lustrous black solid. Density cold-pressed disc: 3.73 g/cm<sup>3</sup>. **ATR-IR:** 2319, 2100 (w, Cu-H); 2026 (m,  $\nu_{B-Ht}$ ); 1975 (m,  $\nu_{B-Hb}$ ); 1036 (m,  $\delta_{BH2}$ ); 429 (w,  $\nu_{\text{Cu-HBH}}$ ) cm<sup>-1</sup>.

### **2.1.3 Cobalt *Borohydride* (Co-BH<sub>4</sub>):**

The same reaction steps and workup procedure were employed using CoCl<sub>2</sub>·6H<sub>2</sub>O (2.379 g, 10 mmol) and NaBH<sub>4</sub> (1.513 g, 40 mmol). Yield = 59%; Color/State: lustrous black

solid. Density cold-pressed disc: 2.24 g/cm<sup>3</sup>. **ATR-IR:** 3354 (br,  $\nu_{\text{O-H}}$ ); 2168, 2071 (m,  $\nu_{\text{B-Ht}}$ ); 2000 (m,  $\nu_{\text{B-Hb}}$ ); 1056 (w,  $\delta_{\text{BH}_2}$ ); 431 (w,  $\nu_{\text{Co-HBH}}$ ) cm<sup>-1</sup>.

#### **2.1.4 Iron Borohydride (Fe-BH<sub>4</sub>):**

A solution of FeSO<sub>4</sub>·7H<sub>2</sub>O (2.78 g, 10 mmol) in 100 mL of H<sub>2</sub>O: DMF (1:1 mixture) was reacted with NaBH<sub>4</sub> (1.513 g, 40 mmol) in 50 mL methanol. The reaction procedure and workup were as described above. FeSO<sub>4</sub>·7H<sub>2</sub>O was used instead of FeCl<sub>2</sub>·6H<sub>2</sub>O to minimize the amount of iron oxide byproducts that might form in the process. Yield = 52%; Color / State: lustrous black solid. Density cold-pressed disc: 2.76 g/cm<sup>3</sup>. **ATR-IR:** 3237 (br,  $\nu_{\text{O-H}}$ ); 2110, 2075 (m,  $\nu_{\text{B-Hi}}$ ); 2001 (m,  $\nu_{\text{B-Hb}}$ ); 1064 (w,  $\delta_{\text{BH}_2}$ ); 420 (w,  $\nu_{\text{Fe-HBH}}$ ) cm<sup>-1</sup>.

### **3.0 Results and Discussion:**

#### **3.1 Formation and Characterization of Transition Metal Borohydrides (M<sub>T</sub>-BHs)**

In general, **M<sub>T</sub>-BHs** are synthesized in various compositions, structures, and properties, as exemplified by their general chemical formula of M<sub>x</sub>(BH<sub>n</sub>)<sub>y</sub> [36,38]. In this work, the desired M<sub>T</sub>-BHs were prepared by mixing the desired metal salt with fourfold excess of NaBH<sub>4</sub> in a nonaqueous DMF/MeOH solvent system, **Equation 5** [38-45]. This complex reaction process is generally affected by the M<sub>T</sub>:BH<sub>4</sub><sup>-</sup> ratio, solvent, pH, and slow/rapid mixing of reagents. Due to the presence of traces of moisture, two main side reactions may be encountered during the reaction, the formation of metallic element (M<sub>T</sub><sup>0</sup>) and metal oxides /borates (M<sub>T</sub>O, M<sub>T</sub>BO<sub>3</sub> **Equation 6** [39, 43,45]. To overcome these possible side reactions, our reactions were carried out in DMF/MeOH solvent mixtures using excess NaBH<sub>4</sub>.



A first look at the obtained thermo-oxidation curves in **Figure 2** suggests that Cu-BH<sub>4</sub> exhibits different behavior from the other three M<sub>T</sub>-BH<sub>4</sub>. Close analysis of Fe-BH<sub>4</sub>, Co-BH<sub>4</sub>, and Ni-BH<sub>4</sub> thermograms shows that Fe-BH<sub>4</sub> is stable below 400 °C while Co-BH<sub>4</sub> and Ni-BH<sub>4</sub> underwent two-step mass losses (~ 20%). At 400-800 °C range, the three M<sub>T</sub>-BH<sub>4</sub> underwent similar two-step dehydrogenation processes to yield the corresponding M<sub>T</sub>-Bs residues (Fe-B, ~81%; Co-B, 68%; Ni-B, 41%). These borides uptake oxygen in the temperature range of 800-1000 °C to yield the corresponding borates (FeBO<sub>3</sub>, 4.7%; CoBO<sub>3</sub>, 12.0; NiBO<sub>3</sub>, 7.4%) where the mass gains represent the oxygen uptake. Upon further heating to 1100 °C, the just-formed M<sub>T</sub>-BO<sub>3</sub> decomposes, eliminating dense white fumes of B<sub>2</sub>O<sub>3</sub>, leaving behind Fe<sub>2</sub>O<sub>3</sub>, Co<sub>2</sub>O<sub>3</sub>, and NiO residues. To ensure complete degradation of M<sub>T</sub>-BO<sub>3</sub>, the resulting residues

**Figure 2: Thermo-oxidative curves of the obtained M<sub>T</sub>-BHs (M<sub>T</sub> = Ni<sup>II</sup>, Fe<sup>II</sup>, Co<sup>II</sup>, Cu<sup>II</sup>).**

were treated three times with deionized water and calcined to a constant weight (1100 °C, one hr.), leaving behind the oxide residues (Fe<sub>2</sub>O<sub>3</sub>, 78.6%; Co<sub>2</sub>O<sub>3</sub>, 72.0%; NiO, 61.9%). The obtained thermo-oxidative data in **Table 1** allowed us to deduce their molecular formula in accordance with the general formula, M<sub>x</sub>(BH<sub>n</sub>)<sub>y</sub>, reported in the literature [35,36,38].

On the other hand, a close look at the thermo oxidative data of Cu-BH<sub>4</sub> shows that the early mass gain (5.6 %) observed at ~250 °C is attributed to the oxidation of the Cu-H phase forming Cu<sub>2</sub>O/CuO [35,39]. This step is followed by the dehydrogenation of Cu-BH<sub>4</sub> phase forming Cu-B (250-500 °C), which consequently oxidized (500-600 °C) to generate the Cu-BO<sub>3</sub> intermediate where it degrades upon further heating (600-900 °C) by releasing B<sub>2</sub>O<sub>3</sub> fumes leaving behind a total mass gain of 7.9% CuO residues. Considering the amounts of CuO

formed due to the Cu-H oxidation early in the process (5.6%); thus, the amount corresponding to oxidation of the Cu-BH<sub>4</sub> phase can be deduced from the difference (2.3%). The molar ratio of these two phases can be calculated from the obtained data and found to be 2.9 Cu<sup>I</sup>-H: 1.0 Cu<sup>II</sup>(BH<sub>4</sub>)<sub>2</sub>, which is consistent with the obtained magnetic data (*vide infra*).

**Table 1:** Thermo-oxidative data and the predicted formula of the investigated M<sub>T</sub>-BHs\*.

M <sub>T</sub> BHs	M <sub>T</sub> -BHs (g)	M <sub>T</sub> -oxide Residue (g)	M <sub>T</sub> : BH <sub>4</sub> mole Ratio	Formula
<b>Fe-BH<sub>4</sub></b>	0.210	0.175	1: 2.7	Fe(BH <sub>4</sub> ) <sub>2.7</sub>
<b>Co-BH<sub>4</sub></b>	0.225	0.185	1: 2.7	Co(BH <sub>4</sub> ) <sub>2.7</sub>
<b>Ni-BH<sub>4</sub></b>	0.240	0.185	1: 2.6	Ni(BH <sub>4</sub> ) <sub>2.6</sub>
<b>Cu-BH<sub>4</sub></b>	0.280	0.300	1: 0.71	2.9 CuH:1Cu(BH <sub>4</sub> ) <sub>2</sub>

\*Mass metal = mass of M<sub>T</sub>O \* (At. mass of M<sub>T</sub>/ molar mass of M<sub>T</sub>O residue). Ni (0.145 g, 00247 mol); Fe (0.122 g, 00219 mol); Co (0.131 g, 00223 mol); Cu (0.240 g, 00378 mol). Mass of BH<sub>4</sub> = mass of M<sub>T</sub>-BHs – mass M<sub>T</sub>; moles BH<sub>4</sub> = mass/molar mass of BH<sub>4</sub>.

### 3.1.2 ATR-IR Spectroscopy of the Prepared M<sub>T</sub>-BHs

The structural complexity of M-BHs is reflected in their FT-IR spectra [46-49]. The ATR-IR vibrational frequencies of the obtained M<sub>T</sub>-BHs and their tentative assignments based on common M-BH<sub>4</sub> and M-H complexes are given in the experimental section and displayed in **Figure 3**. The recorded ATR-IR spectra carry diagnostic evidence that allows the interpretation of relevant structural information about the presence of B-H and M-H bonds. In all cases, the formation M<sub>T</sub>(BH<sub>4</sub>)<sub>x</sub> is evident from the medium intense stretching bands of the terminal ( $\nu_{B-H_t}$ ) and bridging ( $\nu_{B-H_b}$ ) of B-H in the range 2075-2026 cm<sup>-1</sup> and 2026-2002 cm<sup>-1</sup>,

respectively, **Figure 4**. In all cases, the terminal H ( $\nu_{\text{B-Ht}}$ ) stretching bands are associated with shoulders at the high-frequency region of 2100-2320  $\text{cm}^{-1}$  reflecting the presence of different

**Figure 3: ATR-IR spectra of the prepared  $M_{\text{T}}\text{-BHs}$  ( $M_{\text{T}} = \text{Ni}^{\text{II}}, \text{Fe}^{\text{II}}, \text{Co}^{\text{II}}, \text{Cu}^{\text{II}}$ ).**

**Figure 4:** Schematic structure showing terminal and bridging H in  $M\text{-BH}_4$ . coordination modes [46]. The bands due to bending ( $\delta_{\text{BH}_2}$ ) appear in the 1149-1036  $\text{cm}^{-1}$  range. However, the low energy bands due to the stretching vibration of M-H in the four-membered M-H-B-H rings ( $\nu_{\text{M-HBH}}$ ), which typically occur in the low-frequency region of 200-600  $\text{cm}^{-1}$  are observed as weak bands in the 420-470  $\text{cm}^{-1}$  region [39,47-49]. A close look at the ATR spectra of  $\text{Cu-BH}_4$  shows the stretching frequencies of Cu-H at 2100 and 2121  $\text{cm}^{-1}$  [39].

### ***3.1.3 Powder X-Ray Diffraction of the Prepared $M_{\text{T}}\text{-BHs}$ (p-XRD)***

The p-XRD profiles in **Figure 5** were analyzed by inspecting the diffraction patterns, peak position, peak shape, and peak width, which are significant in deducing structural information about the obtained  $M_{\text{T}}\text{-BHs}$ . The profiles are further analyzed for the presence/absence of metallic ( $M_{\text{T}}^0$ ) and metal oxide ( $M_{\text{T}}\text{-O}$ ) impurities common in such preparations. A first look at these profiles shows that their structures vary from highly amorphous  $\text{Fe-BH}_4$  and  $\text{Co-BH}_4$  to predominantly crystalline, as displayed by  $\text{Cu-BH}_4$ . The featureless nature of p-XRD of these  $M_{\text{T}}\text{-BHs}$  is indicative of the formation of vitreous material, which explains their lustrous appearance.

A close inspection of these  $M_{\text{T}}\text{-BHs}$  diffraction patterns shows  $\text{Ni-BH}_4$  and  $\text{Cu-BH}_4$  display sharp diffraction peaks superimposed on broad diffraction features, suggesting vitreous

lattice structures, **Figure 5**. Nevertheless, the co-existence of two different structural phases for Ni-BH<sub>4</sub> and Cu-BH<sub>4</sub> implies that they exhibit clear tendencies to form an amorphous glassy structure upon heat/compression treatment through vitrification/devitrification process bearing in mind the thermal stability of the materials [35,36,40]. On the contrary, Fe-BH<sub>4</sub> and Co-BH<sub>4</sub> analogs exhibit amorphous structures with small broad features at 2 θ of 44.3° and 36.8°, respectively. Close analysis of these diffraction patterns show no detectable amounts of sharp peaks due to metallic Cu<sup>0</sup> (50°), Ni<sup>0</sup> (44°, 52°), Fe<sup>0</sup> (45°, 65°), and Co<sup>0</sup> (41°, 44°, 51°) and their oxides Cu<sub>2</sub>O/CuO (11-20°), NiO (37°,43°,63°), FeO (33°-35°,49°), CoO (33°,37°,62°) which permits us to conclude that no metallic and metal oxides impurities are detected in these M<sub>T</sub>-BHs preparations[35,41,43-45,47].

**Figure 5: P-XRD profiles of the prepared M<sub>T</sub>-BHs (M<sub>T</sub> = Ni<sup>II</sup>, Fe<sup>II</sup>, Co<sup>II</sup>, Cu<sup>II</sup>).**

The diffraction parameters are summarized in **Table 2**. The crystalline phase in the structure was estimated from the area under the broad peaks in the P-XRD profiles. The corresponding interspatial distances (d-spacing) were calculated from the position of the most intense peak as given by Bragg's Law ( $n \lambda = 2 d \sin \theta$ ) where n, λ, and θ are the diffraction order, wavelength of the X-ray beam, and diffraction angle, respectively. The interspatial distances were found to range from 2.04 to 2.47 Å. Furthermore, the crystallite size (t) was calculated as described in the Scherer formula ( $t = K \lambda / \beta \cos \theta$ ) where K (Scherer constant, 0.95), λ (wavelength of the X-Ray), θ (Bragg's angle of the most intense peak) and β (peak width at half-height in radians). It is clear from the crystallite/grain size in **Table 2** that the prepared M<sub>T</sub>-BHs are nano-scaled particles in the range of 6.4-26.2 nm.

**Table 2:** P-XRD data for the investigated M<sub>T</sub>-BHs (M<sub>T</sub> = Ni<sup>II</sup>, Fe<sup>II</sup>, Co<sup>II</sup>, Cu<sup>II</sup>).

M <sub>T</sub> -BHs	Diffraction Angle 2 θ (degrees) <sup>a</sup>	Crystallinity % <sup>b</sup>	d-Spacing (Å) <sup>c</sup>	Grain Size (nm) <sup>d</sup>
<b>Fe-BH<sub>4</sub></b>	14.9-16.3 (55%), 17.8-18.7 (40%), <b>44.3</b> (100%)	~ 4%	2.04	6.4
<b>Co-BH<sub>4</sub></b>	<b>36.8</b> (broad)	~ 1 %	2.44	7.7
<b>Ni-BH<sub>4</sub></b>	12.2-13.4 (28%), 19.9-20.4 (21%), 37.5-38.1 (31%), <b>44.4</b> (100%), 60.9 (26%)	~ 45%	2.04	24.1
<b>Cu-BH<sub>4</sub></b>	35.3 (30%), <b>36.3</b> (100%), 38.6 (5%), 43.1 (25%), 61.3(20%)	~ 73%	2.47	26.2

<sup>a</sup>. The relative peak heights ( $I/I_0$ ) are given in brackets. The most intense peak is given in bold. Here, we report the lines that give a relative intensity of more than 20%.

<sup>b</sup>. Estimated from the area under the diffraction peaks.

<sup>c</sup>. Calculated from  $n \lambda = 2d \sin \theta$ .

<sup>d</sup>. Calculated from Scherer formula ( $t = K \lambda / \beta \cos \theta$ ).

### 3.1.4 Magnetic Characteristics of the Prepared M<sub>T</sub>-BHs

The magnetic characteristics of the prepared M<sub>T</sub>-BHs were investigated using a static magnetic susceptibility method at room temperature. The magnetic data in **Table 3** shows that the determined magnetic moment ( $\mu_{\text{eff}}$ ) per molecular formula for Fe-BH<sub>4</sub>, Co-BH<sub>4</sub>, Ni-BH<sub>4</sub>, and Cu-BH<sub>4</sub> are, respectively, 15.91, 10.98, 5.50, 0.64 BM. Comparing these  $\mu_{\text{eff}}$  values to their  $\mu_{\text{spin}}$  values (Fe<sup>II</sup>, 4.89; Co<sup>II</sup>, 3.87; Ni<sup>II</sup>, 2.83; Cu<sup>II</sup>, 1.73 BM) suggest that Fe-BH<sub>4</sub>, Co-BH<sub>4</sub>, and Ni-BH<sub>4</sub> belong to multi-center systems while but not Cu-BH<sub>4</sub> is an exception. The observed magnetic data for Ni<sup>II</sup>-BH<sub>4</sub> demonstrates that the Ni<sup>II</sup> is situated in an octahedral environment ( $t_{2g}^6 e_g^2$ ) rather than the diamagnetic square planar geometry ( $t_{2g}^6 d_{z^2}^2$ ). Applying the semiempirical scaling laws of  $\mu_{\text{eff}}$  of clusters per magnetic site where their magnetic properties depend on different inherited structural factors, including cluster size, bonding, and geometry, we conclude that Fe-BH<sub>4</sub> and Co-BH<sub>4</sub> belong to trimetallic ferromagnetic aggregates, while

the Ni-BH<sub>4</sub> belongs to bimetallic ferromagnetic class [50,51]. This conclusion is supported by the fact that M<sub>T</sub>-BHs may adopt tetragonal clusters but not layer structures as supported by the P-XRD [26,35-38, 41,44].

On the contrary, the low  $\mu_{\text{eff}}$  value of Cu-BH<sub>4</sub> clusters (0.64 BM) compared to the  $\mu_{\text{spin}}$  value of Cu<sup>II</sup> sites (d<sup>9</sup>, 1.73 BM) suggests that this material comprises diamagnetic Cu<sup>I</sup> (d<sup>10</sup>) centers. This conclusion of biphasic Cu<sup>I</sup>-Cu<sup>II</sup> structure is consistent with the thermo-oxidative that the prepared Cu-BH<sub>4</sub> material comprises Cu-H and Cu(BH<sub>4</sub>)<sub>2</sub> phases. The molar ratio of Cu<sup>I</sup>: Cu<sup>II</sup> calculated from the magnetic data was found to be 2.7: 1, consistent with the molar ratio calculated in the thermo-oxidative section of 2.9: 1.

**Table 3:** Gram magnetic susceptibility ( $\chi_g$ ), effective and spin magnetic moments ( $\mu_{\text{eff}}$ ,  $\mu_{\text{spin}}$ ), magnetic sites per formula, and clustering of the investigated M<sub>T</sub>-BHs (M<sub>T</sub> = Ni<sup>II</sup>, Fe<sup>II</sup>, Co<sup>II</sup>, Cu<sup>II</sup>).

M <sub>T</sub> BHs	$\chi_g$ (10 <sup>6</sup> ) (cm <sup>3</sup> g <sup>-1</sup> ) <sup>a</sup>	$\chi_m$ <sup>a</sup>	$\mu_{\text{eff}}$ (BM) <sup>b</sup>	$\mu_{\text{spin}} / d^n$ (BM) <sup>c</sup>	No. Magnetic Sites <sup>d</sup>	Cluster
Fe-BH <sub>4</sub>	1100	0.1054	15.91	4.89 / d <sup>6</sup>	3.25	Trimetallic
Co-BH <sub>4</sub>	507	0.0502	10.98	3.87 / d <sup>7</sup>	2.84	Trimetallic
Ni-BH <sub>4</sub>	130	0.0126	5.50	2.83 / d <sup>8</sup>	1.94	Bimetallic
Cu-BH <sub>4</sub>	1.83	0.00017	0.64	1.73 / d <sup>9</sup>	0.37	2.7Cu <sup>I</sup> : 1Cu <sup>II</sup> Biphasic

<sup>a</sup>.  $\chi_m$  represents the molar magnetic susceptibility [ $\chi_m = \chi_g * \text{M.wt}$ ], diamagnetic contribution is neglected. Average molecular mass as calculated from thermo-oxidative data. Ni(BH<sub>4</sub>)<sub>2.6</sub>; (97.2 g/mol); Fe(BH<sub>4</sub>)<sub>2.7</sub>; (110.7 g/mol); Co(BH<sub>4</sub>)<sub>2.7</sub> (98.9 g/mol); 2.9 Cu-H :1Cu(BH<sub>4</sub>)<sub>2</sub> (94.7 g/mol).

<sup>b</sup>.  $\mu_{\text{eff}}$  is the effective magnetic moments [ $\mu_{\text{eff}} = 2.83 (\chi_m * T)^{1/2}$ ] at 298 K.

<sup>c</sup>.  $\mu_{\text{spin}} = g[S(S + 1)]^{1/2}$ , g is the gyromagnetic ratio = 2.0023, S total spin.

<sup>d</sup>. The number of magnetic sites per formula is deduced from  $\mu_{\text{eff}} / \mu_{\text{spin}}$ .

<sup>e</sup>. Deduced from the number of metal sites per formula; The Cu-BH<sub>4</sub> comprises two phases containing 2.7 Cu<sup>I</sup>: 1 Cu<sup>II</sup>.

### 3.2 Electrical and Thermal Characteristics of the investigated M<sub>T</sub>-BHs

#### 3.2.1 Electrical Conductivity ( $\sigma$ )

The electrical current (**I**) that develops between the hot and cold brass discs across the prepared  $M_T$ -BHs was examined by plotting their I-V curves, **Figure 6**. The observed nonlinear trend suggests nonohmic behavior observed in diodes, thermistors, heated filaments, and photovoltaic cells where the dynamic resistance is reported to decrease with temperature. This behavior can be attributed to various parameters, the most important of which are the temperature, current density, the time over which the electric field is applied, not to ignore the contribution of the induced ionic conduction [52,53]. Recently, Katsufuji et al. addressed the nonlinear behavior of resistance in various disordered systems and reported that the resistivity decreases as a function of current density /electric field but does not rely on the temperature or the materials. They discussed their observation in the light of the percolation conduction theory in disordered systems [53].

Here, the observed nonlinear curve indicates that the conduction in these  $M_T$ -BHs is not purely electronic but being influenced by different possible factors such as temperature, induced ionization, magnetic field effects, and phonon migration. For that, the nonlinearity of the I-V curves was further analyzed by taking the logarithmic form as described by **Equation 9** and **10** where I, V,  $\alpha$ , and G are the current, voltage, ohmicity, and conductance ( $G = \sigma \times \text{area/thickness}$ ), respectively [54]. The  $\alpha$  can be estimated from the slope of  $\text{Ln}(I) - \text{Ln}(V)$

$$\mathbf{I = V^\alpha * G} \quad \mathbf{(9)}$$

$$\mathbf{\text{Ln}(I) = \alpha \text{Ln}(V) + \text{Ln}(G)} \quad \mathbf{(10)}$$

linear plots in **Figure 6**. The obtained  $\alpha$  values (1.76 - 1.20) substantially deviate from unity ( $\alpha = 1$ ) of pure electronic conduction showing contribution from possible ionic/mass diffusion, **Table 4**. The higher  $\alpha$  factor in the case of Ni-BH<sub>4</sub> (1.76) compared to those of the other studied  $M_T$ -BHs (1.20-1.25) suggests considerable ionic/mass diffusion in Ni-BH<sub>4</sub> thus permitting comparatively large  $\sigma$ , **Table 4**. The determined  $\sigma$  shows that these  $M_T$ -BHs exhibit

semiconducting behavior where Ni-BH<sub>4</sub> shows distinctly higher conductivity than the other three M<sub>T</sub>-BHs.

**Figure 6: I - V and Ln I - Ln V Plots for the examined M<sub>T</sub>-BHs**

**Table 4.** Electrical and thermal conductivity data for the investigated M<sub>T</sub>-BHs.

M <sub>T</sub> BHs <sup>a</sup>	$\alpha$ <sup>b</sup> ohmicity	$\sigma$ <sup>c</sup> Sm <sup>-1</sup>	$\kappa_{tot}$ <sup>d</sup> WK <sup>-1</sup> m <sup>-1</sup>	$\kappa_{el}$ <sup>f</sup> mWK <sup>-1</sup> m <sup>-1</sup>	$\sigma/\kappa$ <sup>e</sup> KV <sup>-2</sup>
Fe BH <sub>4</sub>	1.25	7.0-11.5	1.56-0.18	0.05-0.10	4.5-64.0
Co BH <sub>4</sub>	1.23	5.3-8.6	1.24-0.16	0.04-0.08	4.3-53.8
Ni-BH <sub>4</sub>	<b>1.76</b>	<b>14.7-40.5</b>	<b>1.57-0.18</b>	<b>0.11-0.37</b>	<b>9.4-270</b>
Cu BH <sub>4</sub>	1.20	2.0-2.9	1.26-0.20	0.02-0.03	1.6-14.5

<sup>a</sup> M<sub>T</sub>-BHs disc, 10 ton/cm<sup>2</sup>, radius = 6.51 mm, area,  $\pi r^2 = 1.33 \times 10^{-4}$  m<sup>2</sup>, thickness 1-1.1 mm.

<sup>b</sup>  $\alpha = 1$  for ohmic behavior.

<sup>c</sup>  $\sigma$  (303 ≤ T ≤ 373 K) typical values semiconductors are in the range of 10<sup>-6</sup>-10<sup>4</sup> S m<sup>-1</sup>.

<sup>d</sup>  $\kappa$  (303 ≤ T ≤ 373 K),  $\kappa = Q / [(\Delta T/L) * A]$

<sup>e</sup> Relative contribution of  $\sigma$  to  $\kappa$  (303 ≤ T ≤ 373 K).

<sup>f</sup>  $\kappa_{el}$  were calculated from Wiedemann–Franz law ( $\kappa_{el} = L \sigma T$ ),  $L = 2.44 \times 10^{-8}$  W $\Omega$ K<sup>-2</sup>.

The  $\sigma$  is further investigated as a function of temperature and found that the plot of  $\sigma$  vs. T is linear, **Figure 7**. This increasing trend indicates that the ionic/mass diffusion becomes more prominent while phonon contribution becomes less prominent at higher temperatures. The slope of  $\sigma$  vs. T plots displays a steep linear increase in the case of Ni-BH<sub>4</sub> ( $\sigma = 14.7-40.5$  Sm<sup>-1</sup>), showing increasing charge carrier concentration/mobility and induced ionic/mass conduction compared to the gradual increase observed in the case of Fe-BH<sub>4</sub> ( $\sigma = 7.0-11.5$  Sm<sup>-1</sup>), Co-BH<sub>4</sub> ( $\sigma = 5.3-8.6$  Sm<sup>-1</sup>) and Cu-BH<sub>4</sub> ( $\sigma = 2.0-2.9$  Sm<sup>-1</sup>). The observed enhancement in the electrical data ( $\sigma$  and  $\alpha$ ) of Ni-BH<sub>4</sub> data relative to that of the other three M<sub>T</sub>-BHs can be attributed to ionic/mass mobility.

**Figure 7: Plots of the electrical ( $\sigma$ ) and thermal ( $\kappa$ ) conductivities of the prepared  $M_T$ -BHs as a function of temperature.**

### 3.2.2 Thermal conductivity ( $\kappa$ )

Thermal conductivity ( $\kappa$ ) plays a key role in semiconductors employed in different microelectronic applications. It relies on lattice dynamics, charge carriers, and phonon scattering mechanisms. Herein, the  $\kappa$  ( $\text{WK}^{-1}\text{m}^{-1}$ ) in **Table 4** was determined by examining the heat flux ( $Q$ ) crossing from the hot brass block to the cold brass block through the  $M_T$ -BHs disc in the temperature range of  $303 \leq T \leq 373$  K as depicted in **Equation 11** ( $\Delta T = T_{\text{hot}} - T_{\text{cold}}$  K;  $L$ , thickness in m;  $A$ , area in  $\text{m}^2$ ). The  $\kappa$  values for the given  $M_T$ -BHs slightly varies (1.24-1.57  $\text{WK}^{-1}\text{m}^{-1}$ ) at 310 K but nonlinearly decrease to converge at a common point as they

$$\kappa = Q / [(\Delta T/L) * A] \quad (11)$$

approach 373 K ( $\sim 0.18 \text{ WK}^{-1}\text{m}^{-1}$ ), indicating that  $\kappa$  is inversely proportional to  $T$ , **Figure 7**. These values are close to that reported for layer metal-rich boride of  $\text{PrRh}_{4.8}\text{B}_2$  ( $\kappa = 1.39 \text{ WK}^{-1}\text{m}^{-1}$ ) but lower than that reported for metal-poor borides like  $\text{AlB}_2$  ( $\kappa \sim 100 \text{ WK}^{-1}\text{m}^{-1}$ ), wurtzite  $\text{ZnO}$  ( $50 \text{ WK}^{-1}\text{m}^{-1}$  at room temperature), bulk  $\text{ZnO}$  ( $\sim 100 \text{ WK}^{-1}\text{m}^{-1}$ ), and porous  $\text{ZnO}$  ( $9.65 \text{ WK}^{-1}\text{m}^{-1}$ ) [3,8,9].

However, the thermal heat transfer in TE semiconductors involves multi-transport pathways comprised of an electronic component due to charge carrier migration ( $e^-$  &  $h^+$ ) and phonon scattering due to lattice dynamics [4,55]. Thus,  $\kappa_{\text{total}}$  comprises two main contributions, an electronic ( $\kappa_{\text{el}}$ ) and lattice ( $\kappa_{\text{lat}}$ ) where  $\kappa_{\text{el}}$  is influenced by charge carrier concentration, mobility, their ratio, bipolar interactions, and scattering mechanisms similar to  $\sigma$  while  $\kappa_{\text{lat}}$  is

generally influenced by lattice vibration, **Equation 12** [4,55,56]. Fortunately,  $\kappa_{el}$  can be approximated from the  $\sigma$  values using Wiedemann–Franz law ( $\kappa_{el} = L \sigma T$ ) where  $L$  is the Lorenz number ( $2.44 \times 10^{-8} \text{ W}\Omega\text{K}^{-2}$ ). Although this law is best applied to metal, it is widely employed for semiconductors [4,55]. The calculated  $\kappa_{el}$  data in **Table 4** demonstrates that the

$$\kappa_{\text{total}} = \kappa_{el} + \kappa_{\text{lat}} \quad (12)$$

electronic contributions to  $\kappa_{\text{total}}$  are in the mW/Km range, indicating that the thermal conduction occurs essentially through lattice vibration. In other words, the thermal energy transport in these materials is basically phononic rather than electronic where  $\kappa_{\text{total}} \approx \kappa_{\text{lat}}$ . In this respect, amorphous/ glassy semiconductors, as seen in our case, exhibit low  $\kappa$  as compared with crystalline semiconductors [55,56]. Furthermore, the multi-center clustering and nano-sized  $M_T$ -BHs allow phonons scattering and thus suppress  $\kappa_{\text{lat}}$  in these semiconductors. Therefore, we attribute this observation to the limited mobility of the charge carriers, where they are scattered at the interfacial boundary of the amorphous/vitreous glassy structures.

To gain more insight into the relation between  $\sigma$  and  $\kappa$  in the examined  $M_T$ -BHs, we plotted their ratio  $\sigma / \kappa$  versus  $T$ , **Figure 8**. The  $\sigma / \kappa$  quantitative data in the low and high-temperature ranges examined in this study are listed in Table 4. This ratio plays a vital role in the estimation of TE efficiencies as described  $ZT$  ( $ZT = (\sigma/\kappa) \cdot S^2 \cdot T$ ); therefore, enhancement of this factor relies on boosting  $\sigma$  while suppressing  $\kappa$ . Interestingly, the nonlinear plot increases exponentially, showing a rapid  $\sigma/\kappa$  increase from 9.4 to 270  $\text{KV}^{-2}$  in the  $303 \leq T \leq 373$  K range in the case of Ni-BH<sub>4</sub> while a moderate-weak increase is observed for Fe-BH<sub>4</sub>, Co-BH<sub>4</sub>, and Cu-BH<sub>4</sub>.

**Figure 8: Plots of the  $(\sigma / \kappa)$  versus  $T$  (K).**

### 3.3 Thermoelectric Characteristics of the investigated $M_T$ -BHs

The key parameters that are generally used to characterize TE semiconductors include three parameters, **S**, **PF**, and **ZT**, where their interrelations have been the subject of several theoretical and experimental studies [3,4,16,21,22]. Here, it should be emphasized that the temperature limitation,  $303 \leq T \leq 373$ , in this investigation is governed by the thermo-oxidative stability and our intention to prepare and examine semiconductors for waste heat-current conversion produced by body heat, sunshine, and domestic devices for small-scale TE applications.

The **S** values were evaluated from the slope of their  $\Delta V$  vs.  $\Delta T$  plots, where a slight deviation from linearity is observed, **Figure 9**. Examination of these data shows that at any specified temperature, Ni-BH<sub>4</sub> exhibits higher **S** values (60-80  $\mu\text{VK}^{-1}$ ) than the other three  $M_T$ -BHs (Fe-BH<sub>4</sub>, 30-52; Co-BH<sub>4</sub>, 27-42; Cu-BH<sub>4</sub>, 14-24  $\mu\text{VK}^{-1}$ ), **Table 5**. These **S** coefficients are further analyzed by plotting the individual **S** values as a function of temperature where the

#### **Figure 9: $\Delta V$ vs. $\Delta T$ plots and **S** dependence on temperature for the examined $M_T$ -BHs**

**S vs. T** linear shows positive **S** indicating p-type semiconductors in which the + holes are the primary charge carriers [26,27,35,36]. The obtained **S** values are comparable with those recorded for p- (49  $\mu\text{VK}^{-1}$ ) and n-doped (- 32.6  $\mu\text{VK}^{-1}$ ) graphene films [15,19] while lower than those reported for n-type ZnO (-200  $\mu\text{VK}^{-1}$ ) and nano-porous ZnO (-279  $\mu\text{VK}^{-1}$ ) at room temperature [8,9]. The negative values indicate that the products have n-type semiconducting behavior where the major carriers are electrons.

The performance of TE semiconductors can be evaluated by examining their PF, which is highly influenced by  $\sigma$  and  $S$  parameters ( $PF = \sigma * S^2$ ). **Figure 10** depicts the observed linear plots of **PF vs. T** for the investigated  $M_T$ -BHs where the PF is practically very sensitive to temperature increase in Ni-BH<sub>4</sub> but weakly affected in the case of Fe-BH<sub>4</sub>, Co-BH<sub>4</sub>, and Cu-BH<sub>4</sub>, **Table 5**. Given the trend in  $S$  vs.  $T$  plots where all the four  $M_T$ -BHs show an almost similar increase, the difference in the PF can be attributed mainly to  $\sigma$ . The PF values of Ni-BH<sub>4</sub> ( $259 \mu W m^{-1} K^{-2}$ ) are smaller than that reported for the layer boron-rich YCrB<sub>4</sub> ( $600 \mu W m^{-1} K^{-2}$ ), but higher than that of graphene nanoparticles ( $PF = 3.94 \mu W m^{-1} K^{-2}$ ). The other three  $M_T$ -BHs (Fe-BH<sub>4</sub>, 31.1; Co-BH<sub>4</sub>, 15.2; Cu-BH<sub>4</sub>,  $1.67 \mu W m^{-1} K^{-2}$ ) exhibit similar PF values as those of oxide semiconductors [8-10].

**Table 5.** Thermoelectric parameter data for the investigated  $M_T$ -BHs.

$M_T$ BHs	$S$ ( $\mu V K^{-1}$ ) <sup>a</sup>	$PF$ ( $\mu W m^{-1} K^{-2}$ ) <sup>b</sup>	$ZT$ ( $10^{-2}$ ) <sup>c</sup>	$\eta$ % <sup>d</sup>
<b>Fe-BH<sub>4</sub></b>	30 - 52	4.9 - 31.1	0.12 – 6.4	0.33
<b>Co-BH<sub>4</sub></b>	27 - 42	3.4 - 15.2	0.08 - 3.5	0.19
<b>Ni-BH<sub>4</sub></b>	60 - 80	39.6 - 259	0.76 – 64.4	2.56
<b>Cu-BH<sub>4</sub></b>	14 - 24	0.37 - 1.67	0.01 - 0.28	0.01

<sup>a</sup> Seebeck factor, the range represents the values at 303 & 373 K, respectively.

<sup>b</sup>  $PF = \sigma * S^2$ , the range represents the values at 303 K & 373 K, respectively.

<sup>c</sup>  $ZT = (\sigma/\kappa)*S^2*T$ , the range represents the values at 303 K & 373 K, respectively.

<sup>d</sup> Thermoelectric efficiency,  $\eta$  % =  $(\Delta T/T_h) [(1 + ZT_{avg})^{1/2} - 1] / [(1 + ZT_{avg})^{1/2} + T_c/T_h]$  %

The performance of TE semiconductors can also be deduced from their  $ZT$  values ( $ZT = (\sigma/\kappa) S^2 T$ ), where this parameter relies directly on  $\sigma$ ,  $S$ , and  $T$  but inversely on  $\kappa$ , **Table 5**. The plots in **Figure 10** show that the  $ZT$  values of Ni-BH<sub>4</sub> increase rapidly in a nonlinear

fashion while Fe-BH<sub>4</sub>, Co-BH<sub>4</sub>, and Cu-BH<sub>4</sub> exhibit linear trends with relatively small temperature influence. However, extrapolation of the ZT – T plot of Ni-BH<sub>4</sub> shows it approaches the value ZT = 1 that allows its use for practical application at about 400-450 K. Furthermore, recent reports show that the TE efficiency ( $\eta\%$ ) can be calculated from average ZT values in the specified temperature range as in **Equation 13**. The  $\eta$  efficiency data in Table 5 shows that Ni-BH<sub>4</sub> (2.56%) is far better than those of the other three M<sub>T</sub>-BHs (0.01-0.33%).

$$\eta \% = (\Delta T/T_h) [(1 + ZT_{avg})^{1/2} - 1] / [(1 + ZT_{avg})^{1/2} + T_c/T_h] \% \quad (13)$$

**Figure 10: Power factor (PF) dependence on temperature for obtained M<sub>T</sub>-BHs.**

Given the fact that TE measurements are sensitive to moisture, impurities, particle-particle interactions, and grains orientation within the examined cold-pressed discs, the reported TE values were found to be reproducible within 5-7%. In general, the S, PF, and ZT values for Ni-BH<sub>4</sub> (S, 80  $\mu\text{VK}^{-1}$ ; PF, 259  $\mu\text{W m}^{-1} \text{K}^{-2}$ ; ZT 0.64;  $\eta$ , 2.56% ) were higher than those for the other three M<sub>T</sub>-BHs investigated in this study. Comparison with the TE values of n-doped ZnO nanoparticle at 375 K (S, -279  $\mu\text{VK}^{-1}$ ; PF, 59  $\mu\text{W m}^{-1} \text{K}^{-2}$ ; ZT ~0.075) shows that the Ni-BH<sub>4</sub> offer a promising p-type candidate for TE applications.

**4.0 Conclusions**

The data in this study shows that using organic solvents rather than aqueous media is appropriate to minimize/avoid metal oxide side-products formation in the preparation of metal borohydrides nanoparticles. Unlike the generally observed trends where the thermal and electrical conductivities show similar trends on temperature, the reverse dependence is

observed in the given M<sub>T</sub>-BHs; thus, M<sub>T</sub>-BHs and future M<sub>T</sub>-Bs semiconductors are promising candidates for TE applications. Our findings show that Ni-BH<sub>4</sub> is a promising candidate to convert low-temperature waste heat to electric current resulting from body heat, sunshine, and domestic devices for small-scale applications at ambient conditions. Although the ZT values of the Ni-BH<sub>4</sub> are less than those reported for the present late metal chalcogenides, it is advantageous for its simple preparation, moderate temperature dehydrogenation pathway to form Ni-Bs and applicability at ambient conditions. Our future endeavor is to investigate the influence of magnetic polarization and cold press compression on the TE behavior of Ni-BH<sub>4</sub> and its fluoride analog (Ni-BF<sub>4</sub>).

**Acknowledgments:** The authors highly appreciate the support of the Jordan University of Science and Technology (Grant No. 20200017). The authors acknowledge no conflict of interest.

#### References:

1. J.Y. Tsao, E.F. Schubert, R. Fouquet, M. Lave, The electrification of energy: Long-term trends and opportunities, *MRS Energy Sustain. A Rev. J.*, 5:7 (2018) 1–13. DOI:10.1557/mre.2018.
2. E. Kabir, P. Kumar, S. Kumar, A.A. Adelodun, K.H. Kim, Solar energy: Potential and future prospects, *Renew. Sustain. Energy Rev.*, 82:1 (2018) 894-900.
3. X.-L. Shi, J. Zou, Z.-G. Chen, Advanced Thermoelectric Design: From Materials and Structures to Devices, *Chem. Rev.*, 120 (2020) 7399. DOI: 10.1021/acs.chemrev.0c00026
4. D. Beretta, N. Neophytou, J.M. Hodges, M.G. Kanatzidis, D. Narducci, M. Martin-Gonzalez, M. Beekman, B. Balke, G. Cerretti, W. Tremel, A. Zevalkink, A.I. Hofmann, C. Müller, B. Dörling, M. Campoy-Quiles, M. Caironi, Thermoelectrics: From history, a window to the future, *Mater. Sci. Eng.: R: Reports*, 138 (2019) 100501, doi: 10.1016/j.mser.2018.09.00
5. Z. Zhang, B. Wang, J. Qiu, S. Wang, Roll-to-roll printing of spatial wearable thermoelectrics, *Manuf. Lett.*, 21 (2019) 28 DOI: 10.1016/j.mfglet.2019.07.002

6. X. Shi, J. Yang, J.R. Salvador, M. Chi, J.Y. Cho, H. Wang, S. Bai, J. Yang, W. Zhang, L. Chen, Multiple-filled skutterudites: high thermoelectric figure of merit through separately optimizing electrical and thermal transports. *J. Am. Chem. Soc.* 133:20 (2011) 7837–46. DOI: 10.1021/ja111199y.
7. H. Lipeng, H. Wu, T. Zhu, C. Fu, J. He, P. Ying, X. Zhao, Tuning multiscale microstructures to enhance thermoelectric performance of n-type bismuth-telluride-based solid solutions. *Adv. Energy Mater* 5 (2015) 1500411. DOI: 10.1002/aenm.201500411
8. R.V.R. Virtudazo, Q. Guo, R. Wu, T. Takei, T. Mori, An alternative, faster and simpler method for the formation of hierarchically porous ZnO particles and their thermoelectric performance. *RSC Adv.* 7 (2017) 31960-68. DOI: 10.1039/C7RA05067D
9. X. Wu, J. Lee, V. Varshney, J.L. Wohlwend, A.K. Roy, T. Luo, Thermal Conductivity of Wurtzite Zinc-Oxide From First-Principles Lattice Dynamics--a Comparative Study With Gallium Nitride *Sci Rep.* 6 (2016) 22504. DOI:10.1038/srep22504
10. K. Koumoto, R. Funahashi, E. Guilmeau, Y. Miyazaki, A. Weidenkaff, Y. Wang, C. Wan, Thermoelectric Ceramics for Energy Harvesting. *J. Am. Ceram. Soc.*, 96 (2013) 1–23. DOI:10.1111/jace.12076.
11. J. Liang, S. Yin, C. Wan, Hybrid Thermoelectrics, *Annu. Rev. Mater. Res.* 50 (2020) 319. DOI: 10.1146/annurev-matsci-082319-111001
12. S. Yazdani, M.T Pettes Nanoscale self-assembly of thermoelectric materials: a review of chemistry-based approaches, *Nanotechnology* 29: 43 (2018) 432001, DOI: 10.1088/1361-6528/aad673.
13. Y.Y. Li, Y. Du, Y.C. Dou, K.F. Cai, J.Y. Xu, PEDOT-based thermoelectric nanocomposites—A mini-review. *Synth. Met.* 226 (2017) 119–28. DOI: 10.1016/j.synthmet.2017.02.007
14. J.L. Blackburn, A.J. Ferguson, C. Cho, J.C. Grunlan, Carbon-nanotube-based thermoelectric materials, and devices. *Adv. Mater.* 30:11 (2018) 1704386. DOI: 10.1002/adma.201704386
15. Y. Du, K.F. Cai, S. Shen, Facile preparation, and characterization of graphene nanosheet/polyaniline nanofiber thermoelectric composites. *Funct. Mater. Lett.* 6:5 (2013)1340002. DOI: 10.1142/S179360471340002X
16. Y. Zhang, Y.-J. Heo, M. Park, S.-J. Park, Recent Advances in Organic Thermoelectric Materials: Principle, Mechanisms and Emerging Carbon-Based Green Energy Materials, *Polymers* 11 (2019) 167-89; DOI:10.3390/polym11010167.
17. G. Kim, K.P. Pipe, Thermoelectric model to characterize carrier transport in organic semiconductors. *Phys. Rev. B* 86 (2012) 6709–17.

18. C.Y. Gao, G.M. Chen, Conducting polymer/carbon particle thermoelectric composites: Emerging green energy materials. *Compos. Sci. Technol.* 124 (2016) 52–70. DOI:10.1016/J.COMPSCITECH.2016.01.014
19. K. Kanahashi, M. Ishihara, M. Hasegawa, H. Ohta, T. Takenobu, Giant power factors in p- and n-type large-area graphene films on a flexible plastic substrate. *npj 2D Mater Appl.* 3 (2019) 44. DOI:10.1038/s41699-019-0128-0
20. G. Zhang, Y.-W. Zhang, Thermoelectric properties of two-dimensional transition metal dichalcogenides. *J. Mater. Chem. C* 5 (2017) 7684–98. DOI:10.1039/C7TC01088E
21. D. Li, Y. Gong, Y. Chen, J. Lin, Q. Khan, Y. Zhang, Y. Li, H. Zhang, H. Xie, Recent Progress of Two-Dimensional Thermoelectric Materials *Nano-Micro Lett.*, 12 (2020). DOI: 10.1007/s40820-020-0374-x
22. Z-Hua Ge, L-Dong Zhao, D. Wu, X. Liu, B.-Ping Zhang, J.-Feng Li, J. He, Low-cost, abundant binary sulfides as promising thermoelectric materials, *Materials Today*, 19: 4 (2016) 227-239, <https://doi.org/10.1016/j.mattod.2015.10.004>.
23. P. Mangelis, P. Vaqueiro, A.V. Powell, Improved Thermoelectric Performance through Double Substitution in Shandite-Type Mixed-Metal Sulfides, *ACS Appl. Energy Mater.* 3: 3 (2020) 2168-74. DOI: 10.1021/acsaem.9b02272
24. H. Xi, L. Luo, G. Fraisse, Development and applications of solar-based thermoelectric technologies, *Renew. Sustain Energy Rev.* 11:5 (2007) 923-36. DOI:10.1016/j.rser.2005.06.008
25. Ye, Tao, Xizu Wang, Xianqiang Li, Alex Qingyu Yan, Seeram Ramakrishna, and Jianwei Xu. "Ultra-high Seebeck coefficient and low thermal conductivity of a centimeter-sized perovskite single crystal acquired by a modified fast growth method." *Journal of Materials Chemistry C* 5, no. 5 (2017): 1255-1260.
26. T. Mori Thermoelectric and magnetic properties of rare earth borides: Boron cluster and layered compounds *J. Solid State Chem.* 275 (2019) 70-82. DOI:10.1016/j.jssc.2019.03.046.
27. T. Mori and T. Tanaka, Thermoelectric properties of homologous p-and n-type boron-rich borides. *J. Solid State Chem.* 179: 9 (2006) 2908-15. DOI:10.1016/j.jssc.2006.03.030
28. G. Akopov, L.E. Pangilinan, R. Mohammadi, R.B. Kaner, Perspective: Super-hard metal borides: A look forward, *APL Mater.* 6 (2018) 070901. DOI:10.1063/1.5040763
29. A.-M. Zieschang, J.D. Bocarsly, J. Schuch, C.V. Reichel, B. Kaiser, W. Jaegermann, R. Seshadri, B. Albert, Magnetic and Electrocatalytic Properties of Nanoscale Cobalt Boride, *Co<sub>3</sub>B Inorg. Chem.* 58: 24 (2019) 16609–17, DOI.org/10.1021/acs.inorgchem.9b02617

30. P.R. Jothi, K.Y. Boniface, P.T. Fokwa, A Simple, General Synthetic Route toward Nanoscale Transition Metal Borides, *Adv. Mater.*, 30 : 14 (2018) 1704181, DOI.org/10.1002/adma.201704181.
31. J. Ptačinová, M. Drienovský, M. Palcut, R. Čička, M. Kusý, M. Hudáková Oxidation stability of boride coatings, *Kovove Mater.* 53 (2015) 175–86, DOI: 10.4149/km 2015 3175.
32. B. Jiang, H. Song, Y. Kang, S. Wang, Q. Wang, X. Zhou, K. Kani, Y. Guo, J. Ye, H. Li, Y. Sakka, J. Henzie, Y. Yusuke. A mesoporous non-precious metal boride system: synthesis of mesoporous cobalt boride by strictly controlled chemical reduction. *Chem. Sci.*, 11 (2020) 791-96. DOI: 10.1039/C9SC04498A
33. A.K. Iyer, Y. Zhang, J.P. Scheifers, B. P.T. Fokwa, Structural variations, relationships and properties of  $M_2B$  metal borides, *J. Solid State Chem.*, 270 (2019) 618-35. DOI: 10.1016/j.jssc.2018.12.014
34. C. Kapfenberger, K. Hofmann, B. Albert, Room-temperature synthesis of metal borides. *Solid State Sci.* 5:6 (2003), 925-30. DOI:10.1016/S1293-2558(03)00117-1
35. M. Paskevicius, L.H. Jepsen, P. Schouwink, R. Černý, D.B. Ravnsbæk, Y. Filinchuk, M. Dornheim, F. Besenbacher, T.R. Jensen, Metal borohydrides and derivatives – synthesis, structure and properties, *Chem. Soc. Rev.*, 46 (2017) 1565-34. <https://DOI.org/10.1039/C6CS00705H>
36. W. Lohstroh, M. Heere, Structure and Dynamics of Borohydrides Studied by Neutron Scattering Techniques: A Review, *J. Phys. Soc. Jpn.*, 89 (2020) 051011. DOI: 10.7566/JPSJ.89.051011
37. B. Richter, J.B. Grinderslev, K.T. Møller, M. Paskevicius, T.R. Jensen, From Metal Hydrides to Metal Borohydrides, *Inorg. Chem.* 57 (2018) 10768. DOI: 10.1021/acs.inorgchem.8b01398.
38. J.B. Grinderslev, K.T. Møller, M. Bremholm, T.R. Jensen, Trends in Synthesis, Crystal Structure, and Thermal and Magnetic Properties of Rare-Earth Metal Borohydrides, *Inorg. Chem.*, 58 (2019) 55035517, DOI: 10.1021/acs.inorgchem.8b03258.
39. E.L. Bennett, T. Wilson, P.J. Murphy, K. Refson, A.C. Hannon, S. Imberti, S.K. Clear, G.A. Chass, S.F. Parker, Structure and spectroscopy of CuH prepared via borohydride reduction, *Acta Cryst. B* 71 (2015) 608-12, DOI.org/10.1107/S2052520615015176
40. L. Ma, T. Zhou, H. Chen, Stability and bonding nature of tin borohydride, *Int. J. Hydrogen Energy*, 45 (2020) 23103. DOI: 10.1016/j.ijhydene.2020.06.197.
41. R. Černý, P. Schouwink, The crystal chemistry of inorganic metal borohydrides and their relation to metal oxides *Acta Cryst. B* 71 (2015) 619-40. DOI.org/10.1107/S2052520615015176.

42. I.L. Jansa, G.N. Kalantzopoulos, K. Nordholm, B.C. Hardback, Destabilization of  $\text{NaBH}_4$  by Transition Metal Fluorides, *Molecules* 25:4 (2020) 780, DOI.org/10.3390/molecules25040780.
43. G.N. Glavee, K.J. Klabunde, C.M. Sorensen, G.C. Hadjipanayis, Borohydride Reduction of Nickel and Copper Ions in Aqueous and Nonaqueous Media. Controllable Chemistry Leading to Nanoscale Metal and Metal Boride Particles. *Langmuir* 10 (1994) 4726—30. DOI:10.1021/la00024a055
44. J.D. Kennedy, The Polyhedral Metallaboranes. Part II. Metallaborane Clusters with Eight Vertices and More, *Prog. Inorg. Chem.*, 34 (2007) 211-434. DOI: 10.1002/9780470166352.ch4
45. E.A. Sterling, J. Stolk, L. Hafford, M. Gross, Sodium Borohydride Reduction of Aqueous Silver-Iron-Nickel Solutions: A Chemical Route to Synthesis of Low Thermal Expansion–High Conductivity Ag-Invar Alloys, *Metall. Mater. Trans. A*, 40A, 2009, 1701-09, DOI: 10.1007/s11661-009-9859-4
46. H. Braunschweig, C. Kollann, D. Rais, Transition-Metal Complexes of Boron—New Insights and Novel Coordination Modes *Angewandte Chemie, Int'l Ed.*, 45: 32 (2006), 5254-74. DOI:10.1002/anie.200600506
47. D. Acosta, E.E. Gonzo, H.A. Destéfánis, Borane-Tetrahydrofurane Complex Reduction of Nickel and First Transition Metals in Tetrahydrofurane Media: Controllable Chemistry Leading to Nanoscale Metal and Metal Boride Particle. *Mod. Res. Catal.*, 5 (2016), 19-30. DOI:/10.4236/mrc.2016.51003
48. B. Schrader (ed), *Infrared and Raman Spectroscopy, Methods and Application*, VCH, Weinheim, 1995.
49. N.V. Belkova, I.E. Golub, E.I. Gutsul, K.A. Lyssenko, A.S. Peregudov, V.D. Makhaev, O.A. Filippov, L.M. Epstein, A. Rossin, M. Peruzzini, E.S. Shubina, Binuclear Copper(I) Borohydride Complex Containing Bridging Bis(diphenylphosphino) Methane Ligands: Polymorphic Structures of  $[(\mu_2\text{-dppm})_2\text{Cu}_2(\eta^2\text{-BH}_4)_2]$  Dichloromethane Solvate *Crystals* 7: 10 (2017) 318, DOI:10.3390/cryst7100318
50. C. Li, J. Zhang, W. Zhang, Y. Tang, B. Ren, Y. Hu, First-principle study of structural, electronic, and magnetic properties of  $(\text{FEC})_n$  ( $n = 1-8$ ) and  $(\text{FEC})_8\text{TM}$  ( $\text{TM} = \text{V}, \text{Cr}, \text{Mn},$  and  $\text{Co}$ ) clusters. *Sci Rep* 7 (2017) 17516. doi.org/10.1038/s41598-017-17834-9
51. Y-W. Jun, J-W. Seo, J. Cheon, Nanoscaling laws of magnetic nanoparticles and their applicabilities in biomedical sciences, *Acc. Chem. Res.* 41:2 (2008) 179-89. DOI: 10.1021/ar700121f.
52. W. Ślubowska, K. Becmer, T.K. Pietrzak, J.L. Nowiński, M. Wasiucionek, J.E. Garbarczyk. The charge storage capacity of all-glass heterogeneous materials based on phosphate and vanadate glasses. *Solid State Ionics* 302 (2017) 98-101.

- 53.** T. Katsufuji, H. Ikeda, M. Ashizawa, M. Oike, T. Kajita, Nonlinear Behavior in the Electrical Resistance of Strongly Correlated Insulators, *J. Phys. Soc. Jpn.*, 89 (2020) 044702-5. <https://doi.org/10.7566/JPSJ.89.044702>
- 54.** I.M. Arafa, H.El-Ghanem, R. Al-Shalabi, Formation, Characterization and Electrical Conductivity of Polycarbosilazane-Cu(II), -Ni(II) and -Cr(III) Chloride Metallopolymers, *J. Inorg. Organomet. Polym.* 13 (2003) 69-86. DOI:10.1023/A:1024172613900.
- 55.** M.A. Zoui, S. Bentouba, J.G. Stocholm, M. Bourouis, A Review on Thermoelectric Generators: Progress and Applications, *Energies* 13 (2020) 3606-37; doi:10.3390/en13143606
- 56.** S. Wang, J. Yang, T. Toll, J. Yang, W. Zhang, X. Tang, Conductivity-limiting bipolar thermal conductivity in semiconductors, *Sci. Reports*, 5 (2015) 10136, DOI: 10.1038/srep10136

# Figures

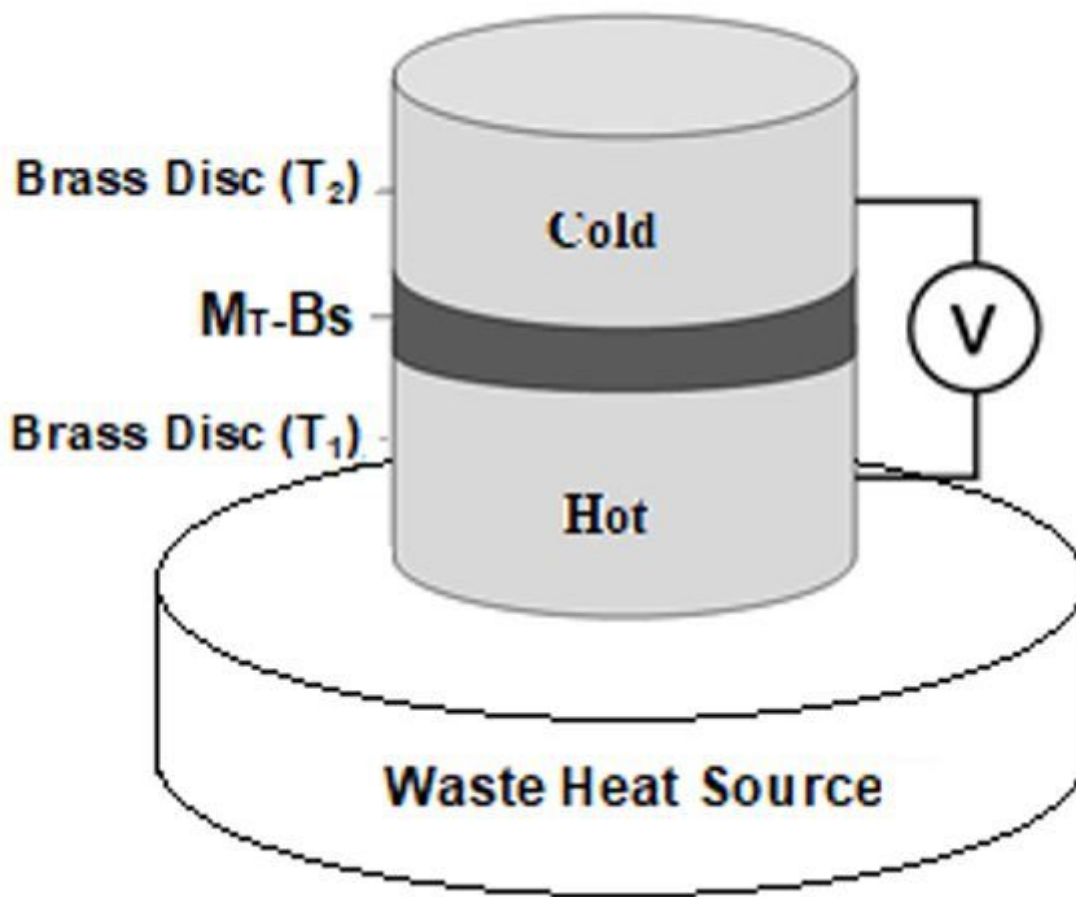


Figure 1

Device for thermoelectric properties.

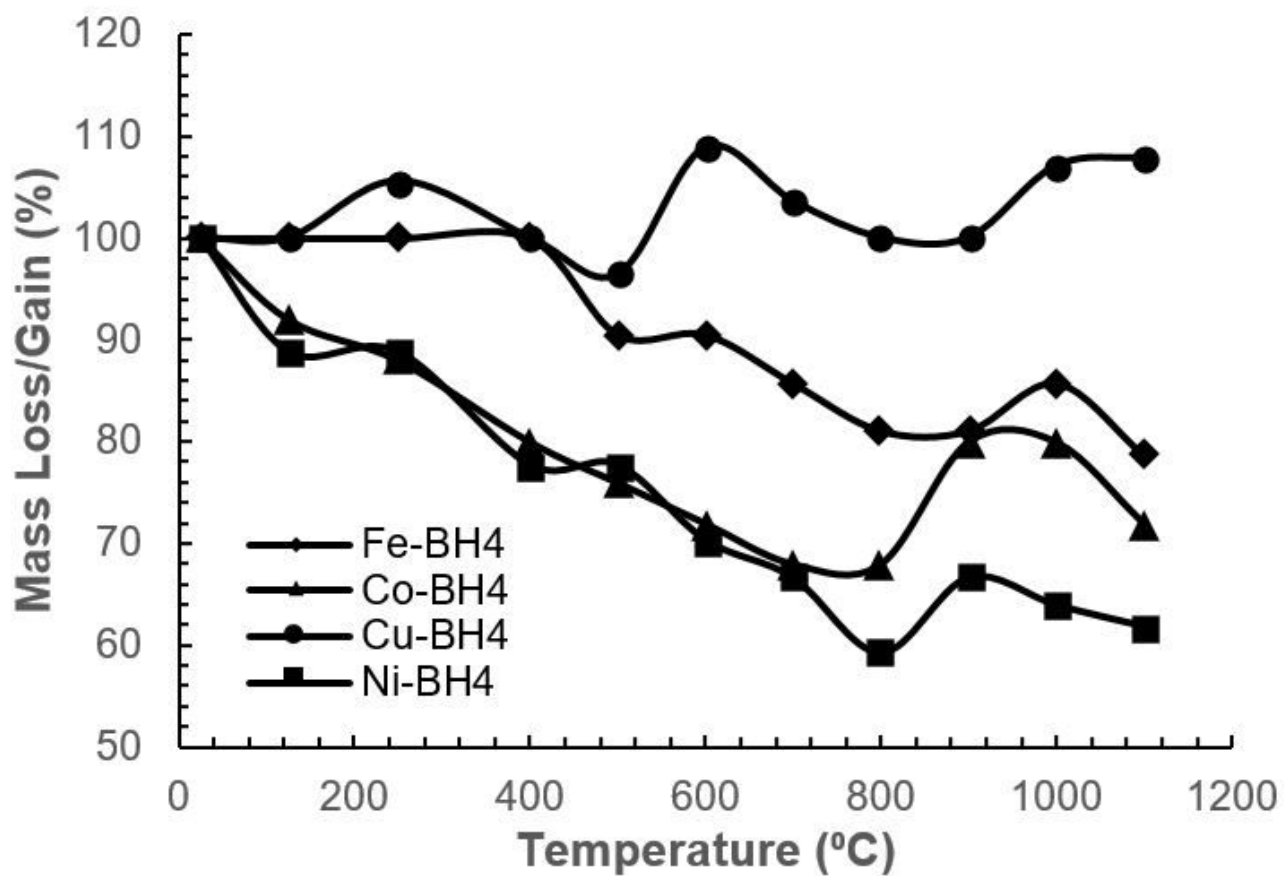


Figure 2

Thermo-oxidative curves of the obtained MT-BHs (MT = NiII, FeII, CoII, CuII).

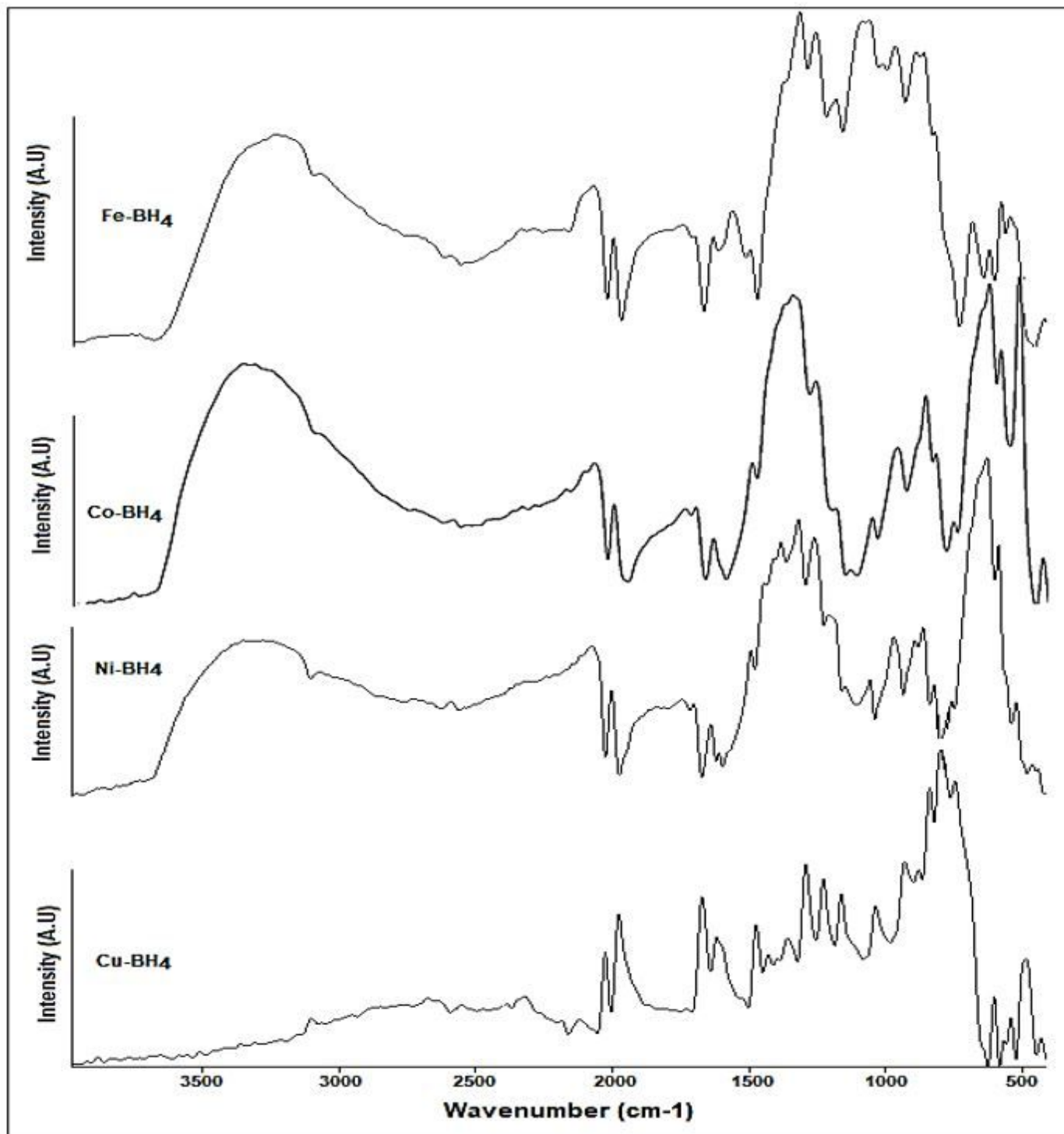


Figure 3

ATR-IR spectra of the prepared MT-BHs (MT = NiII, FeII, CoII, CuI).

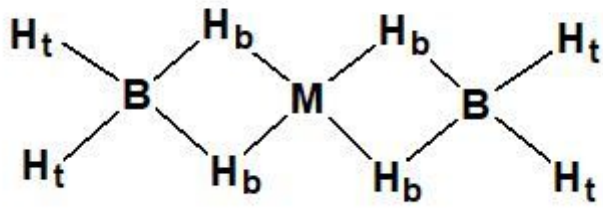


Figure 4

Schematic structure showing terminal and bridging H in M-BH<sub>4</sub>.

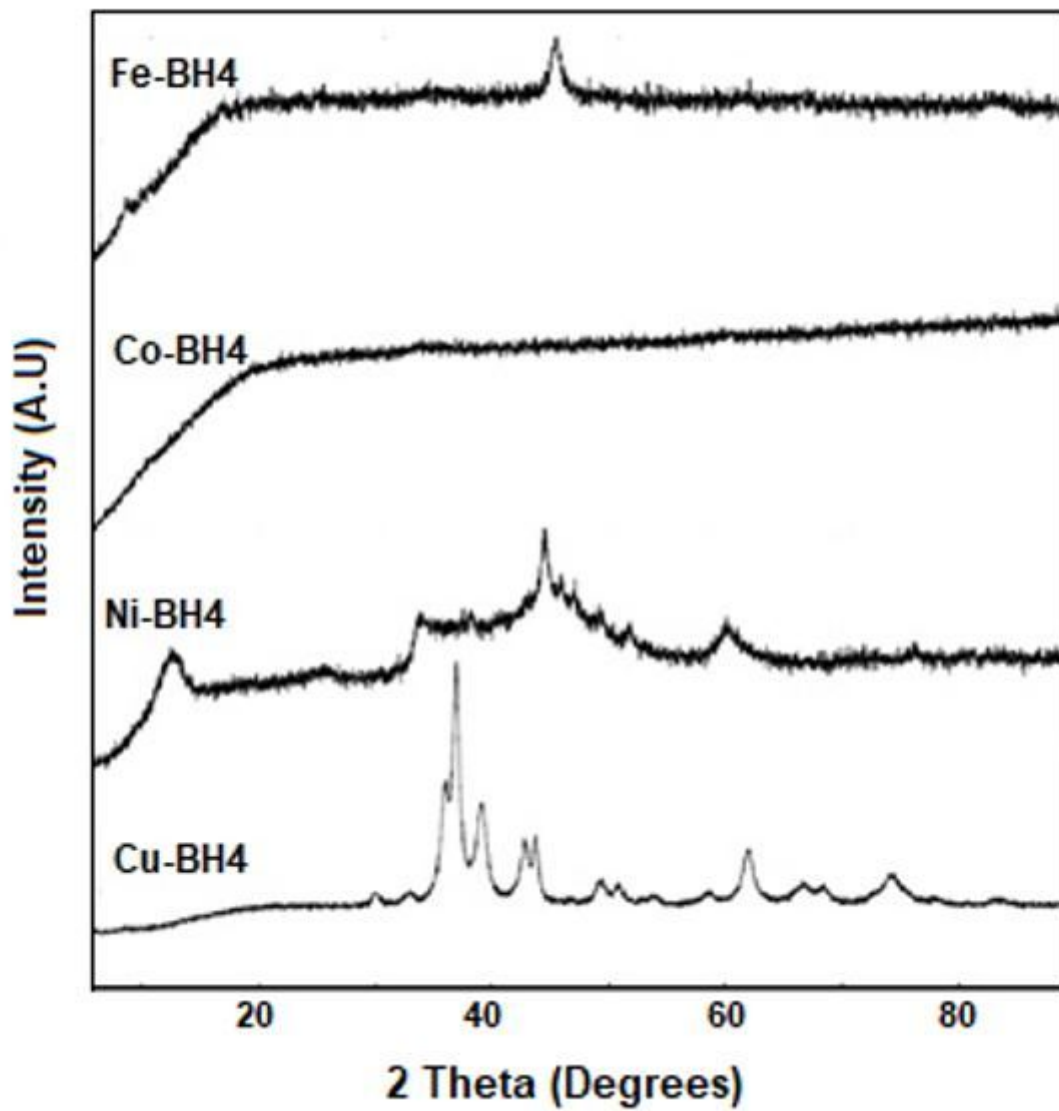


Figure 5

P-XRD profiles of the prepared MT-BH<sub>4</sub>s (MT = NiII, FeII, CoII, CuI).

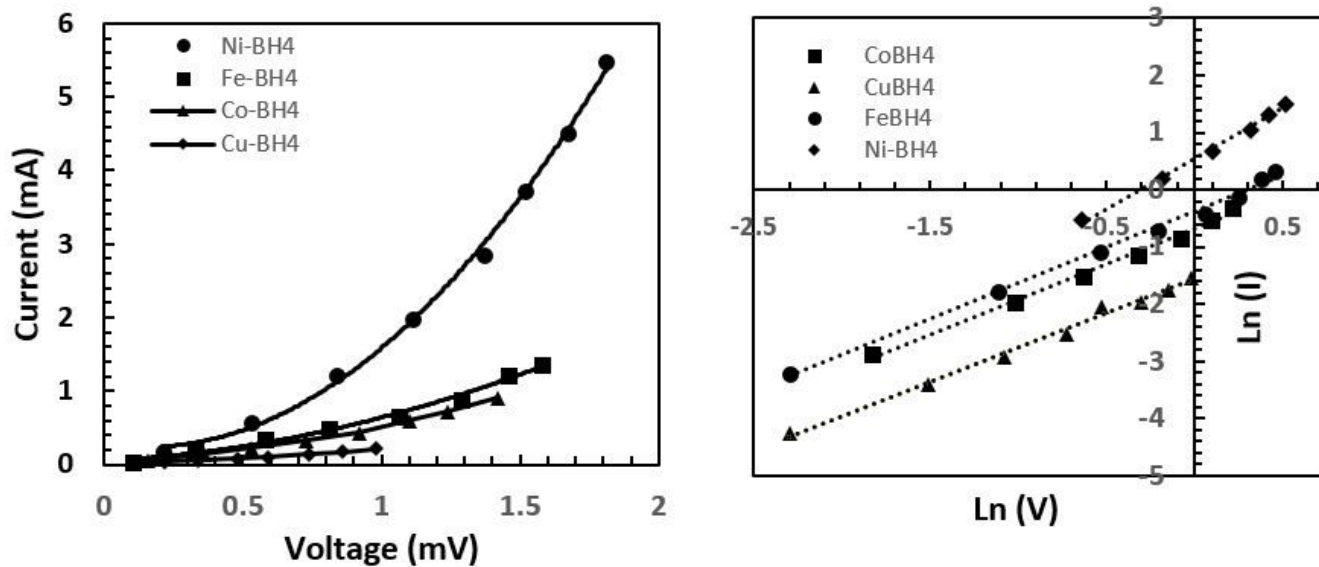


Figure 6

I - V and Ln I - Ln V Plots for the examined MT-BHs

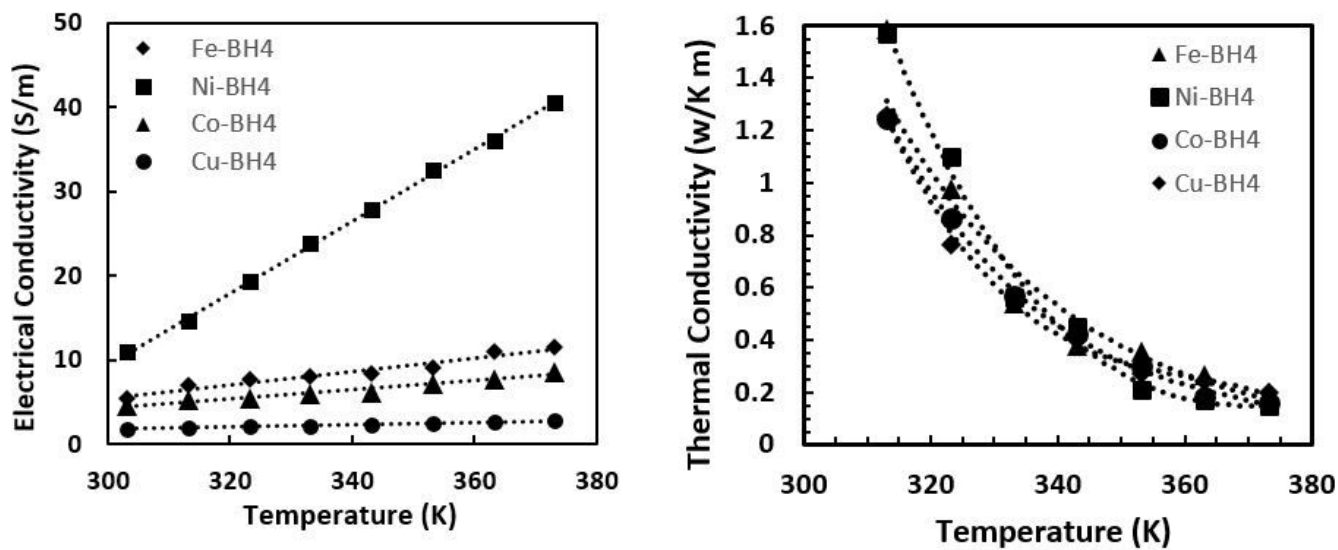


Figure 7

please see the manuscript file for the full caption

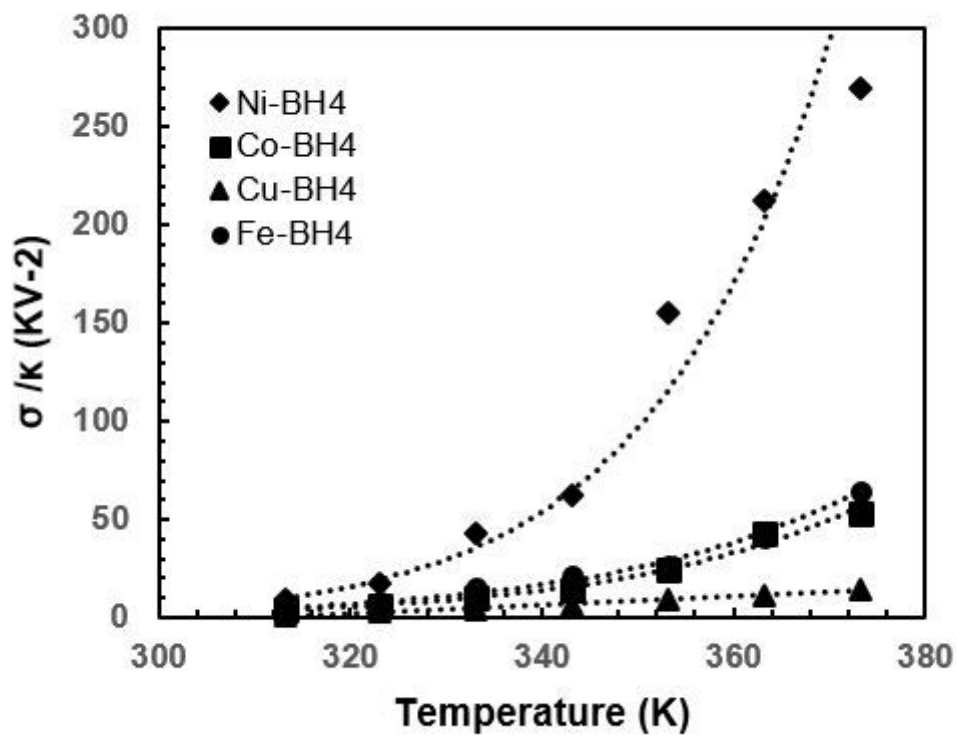


Figure 8

please see the manuscript file for the full caption

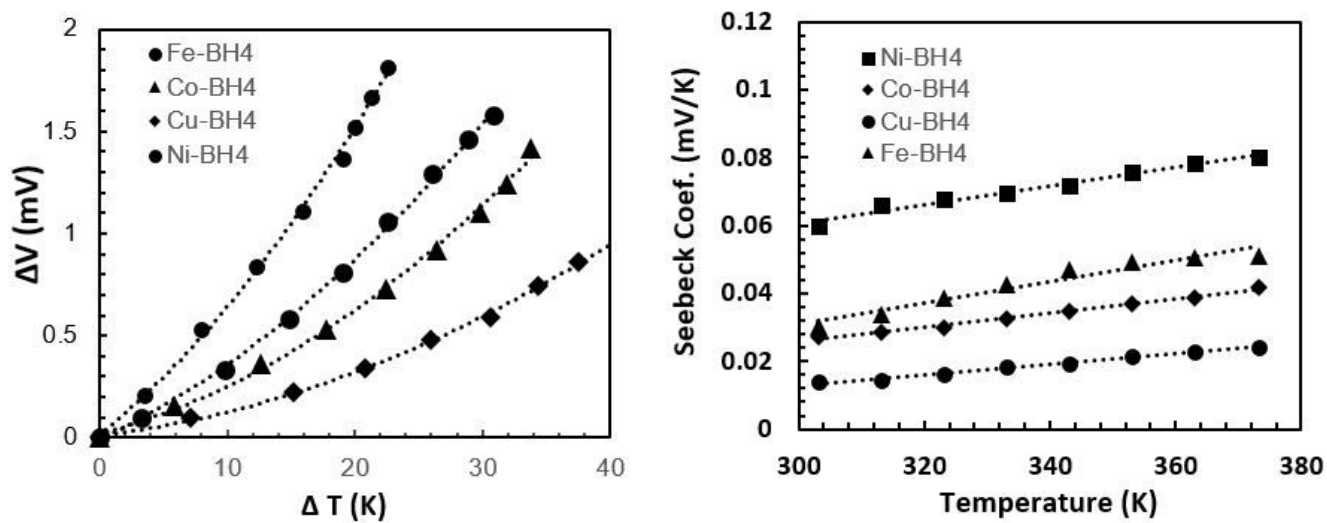


Figure 9

please see the manuscript file for the full caption

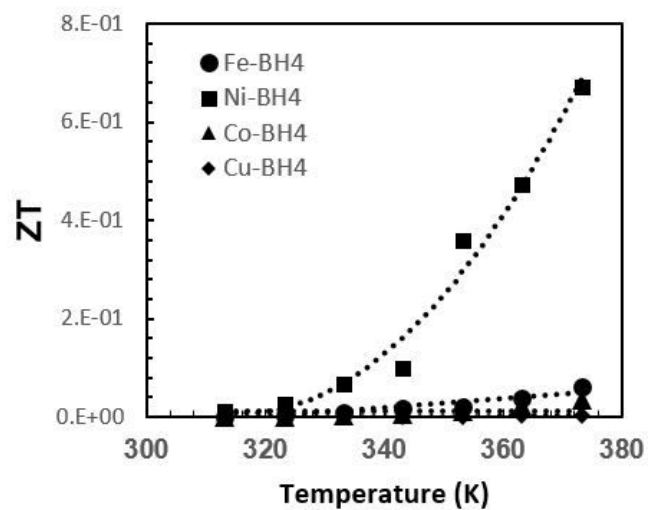
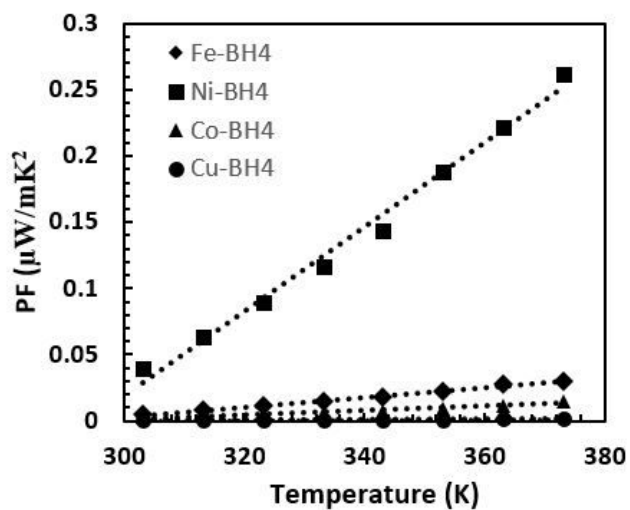


Figure 10

PF and ZT dependence on temperature for obtained MT-BHs.